1 *Type of the Paper: Article*

2 Exploring the influence of the microstructure on the
3 passive layer chemistry and breakdown for some
4 titanium-based alloys in normal saline solution

5 **Nader El-Bagoury[1,2], Sameh Ibrahim[2,4], Ola Ahmed Abu Ali[1], Shimaa El-Hadad[3], Ahmed M.**
6 **Fallatah[1], G.A.M. Mersal[1,5], Mohamed M. Ibrahim[1,6], Joanna Wysocka[7], Jacek Ryl*[7], Rabah**
7 **Boukherroub[8], Mohammed A. Amin*[1,9]**

8 [1] Department of Chemistry, Faculty of Science, Taif University, 21974, Taif, P. O. Box 888, Saudi
9 Arabia

10 [2] Department of Physics, Faculty of Science, Taif University, 888 Hawiya, Saudi Arabia

11 [3] Central Metallurgical Research and Development Institute, P.O. Box: 87 Helwan, Cairo, Egypt

12 [4] Department of Physics, Faculty of Science, Ain Shams University, 11566 Abbassia, Cairo, Egypt

13 [5] Chemistry Department, Faculty of Science, South Valley University, Qena, Egypt

14 [6] Chemistry Department, Faculty of Science, Kafrelsheikh University, 33516, KafrElSheikh, Egypt

15 [7] Department of Electrochemistry, Corrosion and Materials Engineering, Chemical Faculty, Gdansk
16 University of Technology, Narutowicza 11/12, 80-233 Gdansk, Poland

17 [8] Univ. Lille, CNRS, Centrale Lille, ISEN, Univ. Valenciennes, UMR 8520 - IEMN, F-59000 Lille,
18 France

19 [9] Department of Chemistry, Faculty of Science, Ain Shams University, 11566 Abbassia, Cairo, Egypt
20

21   *   Correspondence: jacek.ryl@pg.edu.pl; +48-58-347-1092 (J.R.)
22   maaismail@yahoo.com +966-545-707-507 (M.A.)

23

24 **Abstract:** The effect of microstructure and chemistry of passive films on the kinetics of passive
25 layer growth and passivity breakdown of some Ti-based alloys, namely Ti-6Al-4V, Ti-6Al-7Nb and
26 TC21 alloys was studied. The rate of pitting corrosion was evaluated using cyclic polarization
27 measurements. Chronoamperometry was applied to assess the passive layer growth kinetics and
28 breakdown. Microstructure influence on the uniform corrosion rate of these alloys was also
29 investigated employing Tafel extrapolation and dynamic electrochemical impedance spectroscopy.
30 Corrosion studies were performed in 0.9% NaCl solution at 37 oC, and the obtained results were
31 compared with ultrapure Ti (99.99%). The different phases of the microstructure were
32 characterized by X-ray diffraction and scanning electron microscopy. Chemical composition and
33 chemistry of the corroded surfaces were studied using X-ray photoelectron analysis. For all studied
34 alloys, the microstructure consisted of α matrix, which was strengthened by β phase. The highest
35 and the lowest values of the β phase's volume fraction were recorded for TC21 and Ti-Al-Nb alloys,
36 respectively. The uniform corrosion rate and pitting corrosion resistance (R_{pit}) of the studied alloys
37 were enhanced following the sequence: Ti-6Al-7Nb < Ti-6Al-4V << TC21. The corrosion resistance
38 of Ti-Al-Nb alloy approached that of pure Ti. The obvious changes in the microstructure of these
39 alloys, together with XPS findings, were adopted to interpret the pronounced variation in their
40 corrosion rates.

41 **Keywords:** Titanium-based alloys; Microstructure; Passivity breakdown; Pitting corrosion
42

43

1. Introduction

Titanium and its alloys are widely used in many industrial applications, because of their highly desirable properties, including very good mechanical properties, excellent corrosion and erosion resistance, and favorable strength to weight ratios [1]. In fact, titanium and its alloys have experienced increased use in the past years as biomaterials, because of their superior biocompatibility, high resistance to localized and generalized corrosion, and their good mechanical properties (fatigue resistance) [2]. Among all titanium and its alloys, the commonly used materials in biomedical area are commercially pure titanium (cp Ti) and its (α+ β) Ti6-Al4-V alloy [3–5].

Next to biomedical applications, aerospace sector has dominated titanium use, instead of heavy steel components, in fabricating crucial and decisive systems such as airfoils and airframes [6–9]. About 50% of titanium used in the aerospace industry is the (α+β) alloy Ti-6Al-4V. This alloy possesses a perfect combination of operational and technological properties [10,11]. Titanium alloys have also found widespread applications in a variety of fields such as in chemical and petrochemical sectors due to their excellent corrosion resistance [12]. The outstanding characteristics (such as high specific strength, high fatigue strength, good corrosion resistance, etc.) of the titanium alloys (particularly Ti-6Al-4V) are attributed to a very stable native oxide film (1.5 – 10 nm) formed on the Ti and Ti-alloy surface upon exposure to atmosphere and/or aqueous environments [13,14]. However, this thin oxide layer can be damaged and thus strongly impacts the bioactivity and other characteristics of the material. To improve the performance of Ti and Ti-alloys for biomedical and aerospace applications, oxidation (anodization) has been applied as a successful approach to improve the material properties [15].

The microstructure, formed during various processing methods, is found to greatly affect the mechanical properties of titanium alloys [16]. The microstructure type (bimodal, lamellar and equiaxed) affects the mechanical properties of Ti based alloys [17]. Even though, the corrosion of Ti-alloys in different environments was previously studied [18,19], to the best of our knowledge, literature data revealed no reports concerning the passive layer growth kinetics and breakdown, and subsequent initiation and propagation of pitting corrosion over the surfaces of Ti-6Al-7Nb, Ti-6Al-4V, and TC21 alloys. For this reason, the main objective of this work is to shed more light on the pitting corrosion characteristics of these alloys, employing cyclic polarization and chronoamperometry measurements. In addition, the uniform corrosion behavior of these alloys was also studied based on Tafel extrapolation and EIS methods. All measurements were conducted in 0.9% NaCl solution at 37 ºC.

2. Materials and Methods

The working electrodes investigated in this study consist of three Ti-based alloys, namely Ti-6Al-4V, Ti-6Al-7Nb and TC21; their chemical compositions are presented in **Table 1**. The microstructure of these alloys was studied by Meiji optical microscope fitted with a digital camera. A JEOL JSM5410 and Hitachi S-3400N scanning electron microscopes (SEM) were also used for microstructure studies. For this purpose, the specimens were prepared following ASTM E3-11 standard metallographic procedures, and then etched in a mixture of 5 mL HNO_3, 10 mL HF and 85 mL H_2O. The alloys were machined in the form of rods to perform electrochemical measurements. These rods were mounted in a polyester resin offering an active cross-sectional area of ~ 0.2 cm^2. Prior to conducting any electrochemical analysis, the surface of the working electrode was cleaned and polished using a silicon carbide paper (600-grit) installed on a polishing machine (Minitech 233). The surface was then washed in distilled water. Finally, an absolute ethanol was used for rinsing.

90   **Table 1 -** Chemical composition of investigated Ti alloys

Alloy	Chemical composition, wt %												
	Al	V	Nb	Sn	Zr	Mo	Cr	Si	Fe	C	N	O	Ti
Ti-6Al-4V	5.85	3.94	0.00	0.00	0.00	0.00	0.00	0.00	0.00	0.02	0.03	0.14	
Ti-6Al-7Nb	6.39	0.00	7.78	0.00	0.00	0.00	0.00	0.00	0.00	0.02	0.04	0.12	Bal.
TC21	5.89	0.00	2.41	2.51	1.59	2.27	1.58	0.067	0.05	0.01	0.01	0.13	

91
92   Electrochemical measurements were conducted in a standard, double-walled electrochemical
93   cell with an inner volume capacity of 200 mL. Temperature of the test solution is maintained
94   constant at the desired value by means of a temperature-controlled water bath (FP40-MA
95   Refrigerated/Heating Circulator). The water, after being adjusted at 37 ± 0.1°C, is allowed to circulate
96   through external jacket of the cell. The cover of the electrochemical cell has five openings with
97   different sizes. Such openings were designed to be fitted to the working electrode, counter electrode
98   (a long, coiled platinum wire), reference electrode (KCl-saturated calomel electrode, SCE), a
99   thermometer and a gas inlet/outlet for gas release. The reference electrode is placed in a Luggin
100 capillary, the tip of which is adjusted to be close to the working electrode to minimize iR drop. The
101 cell was connected to a Potentiostat (Autolab PGSTAT30). The test solution was a normal saline
102 (0.9% NaCl). A Millipore Milli-Q water system (18.2 MΩ cm) was used to freshly prepare the saline
103 solution. The salt was of analytical grade and purchased from Sigma-Aldrich.
104   Linear sweep voltammetry (LSV), Tafel plots, and EIS techniques were applied to investigate
105 the uniform corrosion characteristics of the studied alloys. The susceptibility of these alloys to
106 passivity breakdown was evaluated *via* conducting CP and CA measurements. Uniform corrosion
107 measurements were started by stabilizing the working electrode at the rest potential for 2 h,
108 followed by conducting EIS measurements at the respective corrosion potential (E_{corr}) every day for a
109 week of exposure in 0.9% NaCl solution at 37 °C, covering a wide frequency range (100 kHz –10
110 mHz), with 15 mV perturbation amplitude. Uniform corrosion study is ended by constructing Tafel
111 plots *via* sweeping the electrode potential around the Tafel potential ($E = E_{corr} \pm 250$ mV), applying a
112 sweep rate of 1.0 mV s^{-1}. After that, the electrode is removed from the cell (which is cleaned properly
113 and re-filled up with a new fresh test solution), cleaned and polished up to the mirror finish, as
114 described above, and then inserted in the cell for cyclic polarization measurements.
115 Chronoamperometry technique was also applied using a new set of cleaned and polished electrodes
116 submerged in a cleaned cell filled with a new fresh solution.
117   Prior to performing cyclic polarization technique, the working electrode is allowed to stabilize
118 at the rest potential for 2 h, then swept linearly, with a sweep rate of 1.0 mV s^{-1}, starting from a
119 cathodic potential of -2.0 V *vs.* SCE till +8.0 V *vs.* SCE. The potential sweep was then reversed back
120 with the same sweep rate to reach the start point again thus, forming one complete cycle. To
121 conduct chronoamperometry (current *vs.* time) measurements, a two-step route was applied. The
122 working electrode is first held at a starting cathodic potential of -2.0 V *vs.* SCE for 60 s, then polarized
123 towards the anodic direction with a sweep rate of 1.0 mV s^{-1} till the required anodic potential (E_a).
124 Finally, the anodic current was measured versus time (5.0 min) by holding the working electrode at
125 E_a. To ensure results' reproducibility, each run was repeated at least three times, where mean values
126 of the various electrochemical parameters and their standard deviations were calculated and
127 reported.
128   The XRD diffraction patterns were collected for the bulk samples using a SmartLab SE (Rigaku
129 Americas Corporation, USA) X-ray diffractometer with Cu Kα (λ = 1.54056 Å) operated at 40 kV and
130 40 mA. The scanning speed was 0.2°/min and the scanning angle ranged from 20° to 100° in *2θ*.
131 Energy dispersive X-ray spectroscopy (EDS) measurements were utilized in order to determine
132 microstructural composition of investigated alloys as well as evaluate changes in chemistry as a
133 result of exposure to corrosive media. S-3400N SEM was equipped with UltraDry detector from
134 ThermoFisher Scientific. High-resolution X-ray photoelectron spectroscopy (XPS) studies were
135 carried out on an Escalab 250 Xi from Thermofisher Scientific, equipped with Al Kα source. Pass

136 energy was 20 eV and the spot size diameter was 650 μm. Charge compensation was controlled
137 through the low-energy electron and low energy Ar⁺ ions emission by means of a flood gun
138 (emission current: 150 μA, beam voltage: 2.1 V, filament current: 3.5 A). Avantage software
139 (Thermofisher Scientific) was used for deconvolution purposes.

140 3. Results and discussion

141 *3.1. Microstructure investigation*

142 Based on the morphology of α phase, the microstructure of titanium alloys can be classified into
143 equiaxed, lamellar and bi-modal microstructures *[20]*. The microstructure of Ti-based alloys can be
144 controlled based on their chemical composition, or in other words, based on the balance between the
145 α phase stabilizing elements, such as Al, Sn and O, and the forming β phase elements like V, Mo and
146 Nb *[21]*. As shown in **Fig. 1**, the microstructure of all studied titanium alloys consists of bimodal
147 structure of α/β phases. The initial microstructure of Ti-Al-V and Ti-Al-Nb alloys in as-received
148 (forged) state is represented by equiaxed grains of primary α-phase (dark), as well as β-transformed
149 structure (light), as it can be seen in **Fig. 1**. The β phase formed in the microstructure of both alloys is
150 globular in shape, but seems larger in size in Ti-Al-V alloy than in Ti-Al-V alloy. The particle size of
151 β phase in Al-Ti-V alloy is about 0.5 to 1.5 μm; however its size in Ti-Al-Nb alloy reaches about 0.25
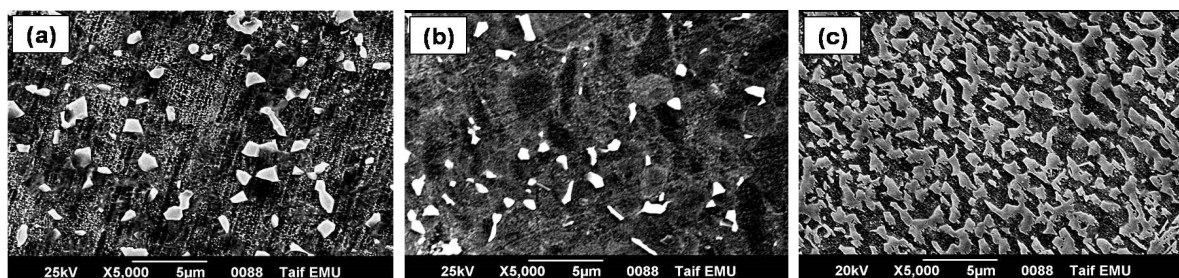152 to 1 μm, as shown in **Fig. 1 (a)** and **(b)**.

153

Figure 1. Microstructure of the three investigated Ti alloys: (**a**) Ti-Al-V, (**b**) Ti-Al-Nb and (**c**) TC21.

158 Similar to Ti-Al-V and Ti-Al-Nb alloys, the microstructure of TC21 alloy, **Fig. 1 (c)**, contains α
159 and β phases, but displays different morphologies and volume fractions. The TC21 alloy's β phase
160 consists of two shapes; the first one is acicular-like structure, **Fig. 2 (a)**, while the other one is a
161 blocky shape, **Fig. 2 (b)**. The thickness of the acicular β phase in the TC21 alloy's microstructure is
162 ranging from around 0.2 to 0.6 μm, while the size extent of the blocky β phase is about 0.75 to 1.5 μm.
163 Moreover, the volume fraction of β phase in the microstructure of TC21 alloy is higher than that in
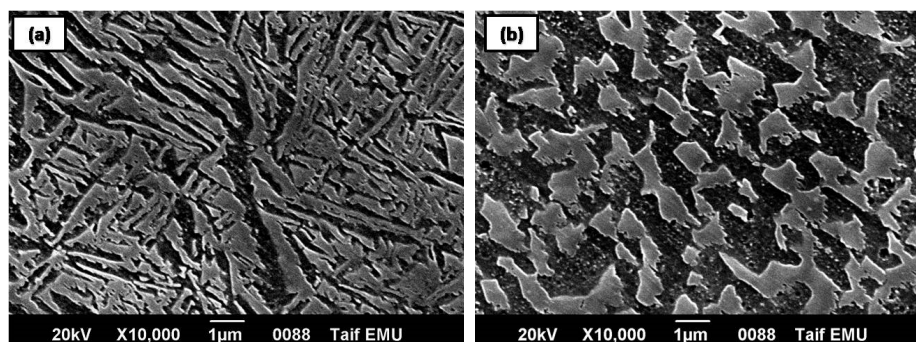164 the Ti-Al-V and Ti-Al-Nb alloys' microstructure, as depicted in **Fig. 1**.

165

Figure 2 - Morphology of β phase in TC21 alloy: (**a**) acicular-like structure and (**b**) blocky shaped
structure

170

171   **Table 2** illustrates the volume fraction of α and β phases in the microstructure of the studied
172   titanium alloys. The microstructure of pure Ti has the highest volume fraction of the α phase (~100%)
173   and the lowest volume fraction of β phase (~0.0%). The presence of Al (α-phase stabilizer) and V
174   (β-phase stabilizer) as alloying elements in the chemical composition of Ti-Al-V alloy influence the
175   volume fraction of α and β phases. The values of the volume fractions of α and β phases (**Table 2**) in
176   the microstructure of Ti-Al-V alloy were 65% and 35%, respectively. Replacing V with Nb, yielding
177   Ti-Al-Nb alloy, resulted in an obvious enhancement in the volume fraction of α phase (increased to
178   77%) at the expense of that of the β phase, which decreased to 23%, as shown in **Table 2**. The volume
179   fraction of both phases in the microstructure of TC21 alloy is also altered, most probably due to the
180   mutual combination of the alloying elements of that alloy, revisit **Table 1**. The volume fractions of α
181   and β phases in the microstructure of TC21 alloy recorded almost equal values, namely 48% for α
182   phase and 52% for β phase (**Table 2**).
183
184   **Table 2 -** Volume fraction of α and β phases in the investigated Ti based alloys.

Alloy	Volume fraction, %		(α/ β) ratio
	α phase	β phase	
Pure Ti	100	0	--
Ti-6Al-4V	65	35	1.86
Ti-6Al-7Nb	77	23	3.35
TC21	48	52	0.92

185
186   To further assess the influence of chemical composition on the microstructure and volume
187   fraction of α and β phases, $[Al]_{eq}$ and $[Mo]_{eq}$ were calculated, where $[Al]_{eq}$ and $[Mo]_{eq}$ represent the
188   alloying elements form α and β phases *[5,22]*. **Table 3** illustrates the calculated values of $[Al]_{eq}$ and
189    $[Mo]_{eq}$ for the tested Ti-based alloys, following Eqs. 1 and 2 *[5,22]*.
190

$$[Al]_{eq.} = [Al] + 0.33[Sn] + 0.17[Zr] + 10[O+C+2N] \qquad (1)$$
$$[Mo]_{eq.} = [Mo] + 0.2[Ta] + 0.28[Nb] + 0.4[W] + 0.67[V] +1.25[Cr] + 1.25[Ni] +$$
$$+ 1.7[Mn] + 1.7[Co] + 2.5[Fe] \qquad (2)$$

194
195   **Table 3 -** $[Al]_{eq}$ and $[Mo]_{eq}$ for the investigated alloys [22,23].

Alloy	$[Al]_{eq}$	$[Mo]_{eq}$	Ratio
TiAlV	8.05	2.64	3.05
TiAlNb	8.59	2.18	3.94
TC21	8.59	5.04	1.71

196
197   It follows from **Table 3** that TiAlNb and TC21 alloys recorded the highest values of $[Al]_{eq}$, 8.59,
198   while the lowest values were measured for the TiAlV alloy, 8.05. Additionally, TiAlNb alloy
199   achieved the maximum value of $[Mo]_{eq}$, 3.94, whilst TC21 alloy recorded 1.71. **Table 3** also depicts
200   the ratio $[Al]_{eq}/[Mo]_{eq}$ for the tested alloys. TiAlNb alloy displayed the maximum ratio, 3.94, while a
201   minimum ratio of 1.71 was measured for the TC21 alloy. It is obvious that the results obtained from
202   **Table 3** agree well with the results in **Table 2**. The calculated ($[Al]_{eq}/[Mo]_{eq}$) and (α/β) ratios are
203   maximum in case of TiAlNb alloy, and minimum for the TC21 alloy.
204   The chemical composition of both phases in all microstructures of the investigated alloys was
205   analyzed using the EDS unit attached to SEM. The EDS spectrum recorded for β phase in the
206   microstructure of Ti-Al-V alloy is depicted in **Figure S1 (b)** (**Supporting Information**). The location
207   of the area of analysis is illustrated in **Figure S1 (a)**. The highest peak in the spectrum belongs to the
208   base metal (Ti), in addition to some other peaks from Al and V alloying elements. Similarly, the
209   analyses of the two phases in other microstructures were accomplished. Results of these analyses are

210   depicted in **Tables 4** and **5**. From the results in **Tables 4** and **5**, it is evident that the Ti, Al, Sn and Zr
211   elements tend to segregate to α phase than to β phase *[23]*. However, V, Nb, Cr and Mo are β
212   forming elements *[24]*, meaning that higher ratios of these elements are found in β phase rather than
213   in α phase.
214
215   **Table 4 -** Chemical composition (wt %) of different phases in Ti-Al-V and Ti-Al-Nb alloys.

Phase	Ti-Al-V alloy (wt %)			Ti-Al-Nb alloy (wt %)		
	Al	V	Ti	Al	Nb	Ti
α	5.93	3.24	90.83	6.60	7.65	85.75
β	5.57	8.04	86.39	4.88	13.79	81.33

216

217   **Table 5 -** Chemical composition (at %) of different phases in TC21 alloy.

Phase	Chemical composition, at %						
	Al	Cr	Mo	Sn	Zr	Nb	Ti
α	6.38	1.08	1.82	2.45	1.95	1.98	84.34
β	6.21	1.71	2.62	2.24	1.11	2.39	83.72

218
219   The line analysis through β phase is shown in **Figure S2** (**Supporting Information**). The phase
220   β is surrounded by the equiaxed α phase in the microstructure of Ti-Al-Nb alloy. The distribution of
221   different alloying elements, Ti, Nb and Al, is illustrated throughout these two phases. The highest
222   line, in green color, represents the distribution of Ti and the grey line shows that of Nb. Additionally,
223   the third one, in pink color, displays the line analysis of the Al element. Obviously, the β phase has
224   lower Ti and Al contents than the α phase, while it has higher amount of Nb compared to α phase.
225   The distribution of alloying elements such as Ti, Al and Nb in Ti-Al-Nb alloy is depicted in **Figure S3**
226   (**Supporting Information**). Mapping analysis for the bimodal α/β microstructure of Ti-Al-Nb alloy
227   is exhibited in **Figure S3 (a)**, **Supporting Information**, where a clear β phase surrounded by
228   equiaxed α phase is observed at higher magnification, 20000×. **Figure S3 (b-d)**, **Supporting**
229   **Information**, illustrates the segregation of Ti, Al and Nb alloying elements, respectively. The
230   distribution of these elements between α and β phases is represented by the density of different
231   colors. The rich areas of Ti, Al and Nb elements are decorated by red color, while the poor areas are
232   painted with dark color. In case of Ti element, as it preferably segregated to α phase, as shown in
233   **Figure S2** (**Supporting Information**), the area of α phase is colored with a combination of red,
234   yellow and pink, however the β phase area, with lower Ti content, has a dark color, see **Figure S3**
235   **(b)**, **Supporting Information**. The contrast for the partitioning of Al alloying element between α and
236   β phases is not as clear as in the case of Ti element, **Fig. S3 (c)**, **Supporting Information**. In addition
237   to the distribution of Ti and Al, the segregation of Nb alloying element, with lower percentage, to α
238   phase is represented by a combination of green, blue and black colors, while the area of the β phase
239   with higher Nb content is decorated by a mixture of red and white colors, as shown in **Figure S3 (d)**,
240   **Supporting Information**.

241   *3.2. X-Ray diffraction studies*

242   Phase identification was performed by X-ray diffraction (XRD) patterns to define the phases
243   comprising each alloy sample. The diffraction patterns recorded for the studied alloys are compared
244   all together in **Fig. 3**. The phases were identified by matching the characteristic peaks with the
245   JCPDS files *[25]*. The phases α-Ti (JCPDS#00-044-1294), β-Ti (JCPDS#00-044-1288) were common and
246   dominated the composition of the three studied alloys. The Ti-Al-V and TC21 alloys were found to
247   contain solely α-Ti and β-Ti phases, respectively. On the other hand, Ti-Al-Nb alloy contained some
248   Ti and Nb oxides, TiO (JCPDS#00-008-0117) and Nb_6O (JCPDS#00-015-0258).
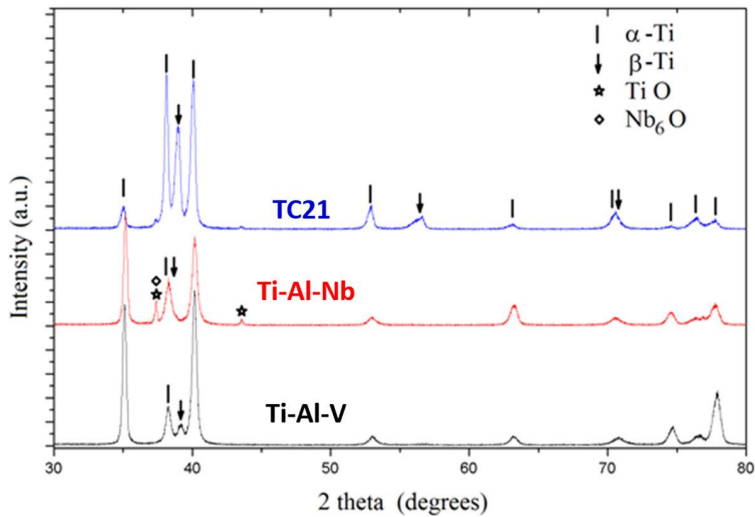249

Figure 3 - XRD diffraction patterns recorded for the samples Ti-6Al-4V, Ti-6Al-7Nb and TC21.

Table 6 - The structural and microstructural parameters of the three alloys obtained by the Rietveld adjustment of the XRD patterns.

	Ti-6Al-4V			
	α-Ti ($P6_3/mmc$)	β-Ti ($Im\bar{3}m$)		
Wt%	67(5)	33(5)		
a (A)	2.9338(1)	3.2353(9)		
c (A)	4.6780 (3)			
D (nm)	76(3)	67(4)		
ε	0.00232(1)	0.00216(4)		
	Ti-6Al-7Nb			
	α-Ti ($P6_3/mmc$)	β-Ti ($Im\bar{3}m$)	TiO ($Fm\bar{3}m$)	Nb6O ($P42cm$)
Wt%	73(6)	20(5)	5(2)	2(1)
a (A)	2.9397(4)	3.2437(5)	4.1567(1)	3.3945(6)
c (A)	4.6969(3)			3.249(3)
D (nm)	67(2)	53(2)	79(12)	100(2)
ε	0.0028(1)	0.024(20)	0.0026(1)	0.00010(7)
	TC21			
	α-Ti ($P6_3/mmc$)	β-Ti ($Im\bar{3}m$)		
Wt%	49(9)	51(9)		
a (A)	2.9407(7)	3.2521(14)		
c (A)	4.6925(16)			
D (nm)	63(2)	70(3)		
ε	0.0021(2)	0.0035(3)		

An effective procedure for the simultaneous refinement of structural and microstructural parameters based on the integration of Fourier analysis for broadened peaks in the Rietveld method was first proposed by Lutterutti et al. *[26]* and is implemented in the Maud program *[27]*. Consequently, weight percent (wt.%), lattice parameters, isotropic crystallite size (D) and r.m.s microstrain (με) were then regarded as fitting parameters in the Rietveld adjustments and were refined altogether simultaneously. The structural information for all the refined phases was obtained

262   from the ICSD database *[28]*. The results obtained for the structural and microstructural analysis are
263   summarized in **Table 6** for all alloys. It is worth to mention here that, all studied alloys were
264   characterized with considerable degree of preferred orientation which strongly modified the relative
265   intensities of the Bragg reflections, especially for α-Ti and β-Ti phases. The MAUD program also
266   incorporates correction for preferred orientation *[29,30]* in the Rietveld adjustments in order to
267   obtain the best fitting parameters.
268   The calculated diffraction patterns from the Rietveld adjustment are plotted with the observed
269   ones for the three alloys in **Fig. 4**. The average R-values obtained for the refinements were about
270   Rwp(%) = 24 to 27 and Rb(%) = 15 to 20. The simultaneous refinements of both structural and
271   microstructural parameters produced good matching of the calculated to observed profiles of
272   diffracted intensities. Also, the incorporation of the preferred orientation models enabled to account
273   for the variations of the peak intensities of α and β-Ti phases.
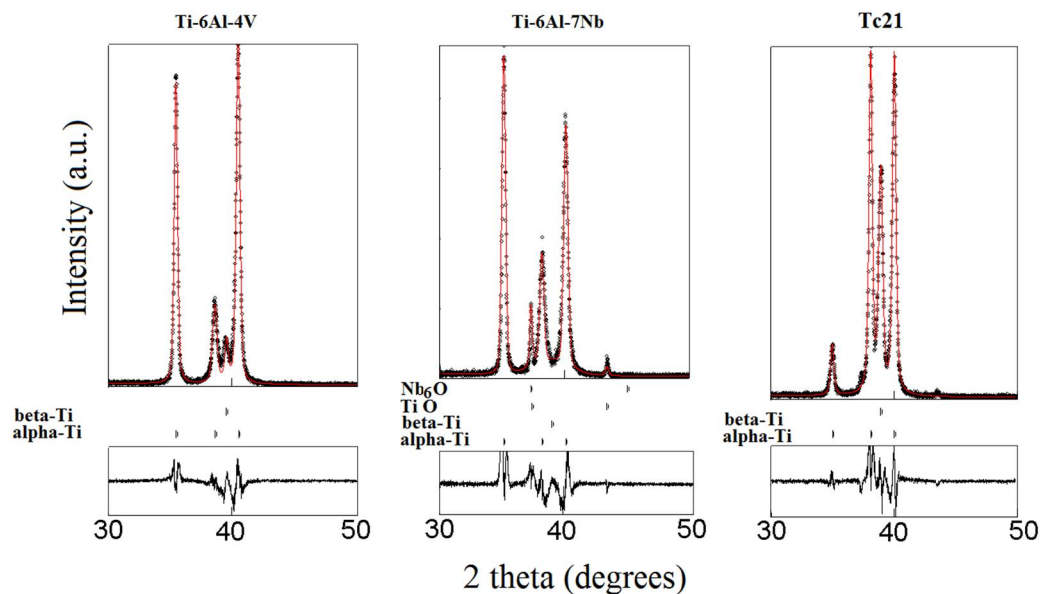274

275
276   **Figure 4 -** The calculated (red line) and observed (black dots) diffraction patterns for the three alloys
277   as obtained from the Rietveld adjustments using the MAUD program; the positions of the Bragg
278   reflections of each phase and the difference between the calculated and observed patterns are also
279   presented at the bottom.
280

281   In the Rietveld adjustment of the alloy Ti-Al-V, the hcpα-Ti (Space group $P6_3/mmc$) together
282   with the bcc β-Ti (Space group $Im\overline{3}m$) dominated the composition of the alloy. In the second alloy,
283   Ti-Al-Nb, the formation of some TiO (Space group $Fm\overline{3}m$) and Nb_6O (Space group $P42cm$) was
284   observed and they form larger crystallites than those formed in the Ti phases. The total weight
285   percent of those oxide phases is less than 10% (**Table 6**). For the third alloy, TC21, only α and β-Ti
286   phases were observed in the XRD patterns. No oxide phases were detected due to the slight oxygen
287   content of this alloy. Nevertheless, there are some mismatches between the wt% values obtained
288   from the Rietveld adjustments and the corresponding wt% values obtained with other techniques.
289   This can be attributed to the behavior of the preferred orientation of the α-Ti phase observed for the
290   reflection (100), which was relatively stronger for the Ti-6Al-4V and Ti6Al7Nb alloys than in the
291   TC21 alloy.
292   As can be seen from **Table 6**, the last two alloys, Ti-Al-Nb and TC21, contain relatively higher
293   portions of β-Ti than α-Ti in contrast to the first alloy, Ti-Al-V, which has α-Ti content higher than
294   β-Ti. As known from literature, Al is an α-stabilizing while V, Nb, Mo and Fe are β-stabilizing.
295   Nevertheless, the results indicate that Nb, Mo and Fe have stronger capabilities to stabilize β-Ti
296   phase than V. These findings corroborate microstructural studies (revisit section 3.1).
297

298   *3.3. Electrochemical measurements*

299   3.3.1.Uniform corrosion studies

300   **Figure 5** illustrates the Tafel plots for the cathodic and anodic domains for the studied alloys in
301   comparison with pure Ti, after 7 days of immersion in 0.9% NaCl solution at 37 °C. **Table 7** depicts
302   the various electrochemical parameters derived from such polarization measurements. It follows
303   from **Fig. 5** that, among the studied alloys, TC21 alloy exhibited the lowest cathodic and anodic
304   overpotentials, corresponding to increased corrosion current density (j_{corr}) values. This is clear from
305   **Table 7**, which revealed that TC21 alloy recorded a j_{corr} value of 0.32 mA cm^{-2}, which is 940, 640, and
306   320 times greater than those measured for pure Ti (3.4×10^{-4} mA cm^{-2}), Ti-Al-Nb (5×10^{-4} mA cm^{-2}),
307   and Ti-Al-V alloys (10^{-3} mA cm^{-2}), respectively. These findings reveal that the rate of the uniform
308   corrosion of the studied alloys increases following the order: Ti < Ti-Al-Nb < Ti-Al-V << TC21.
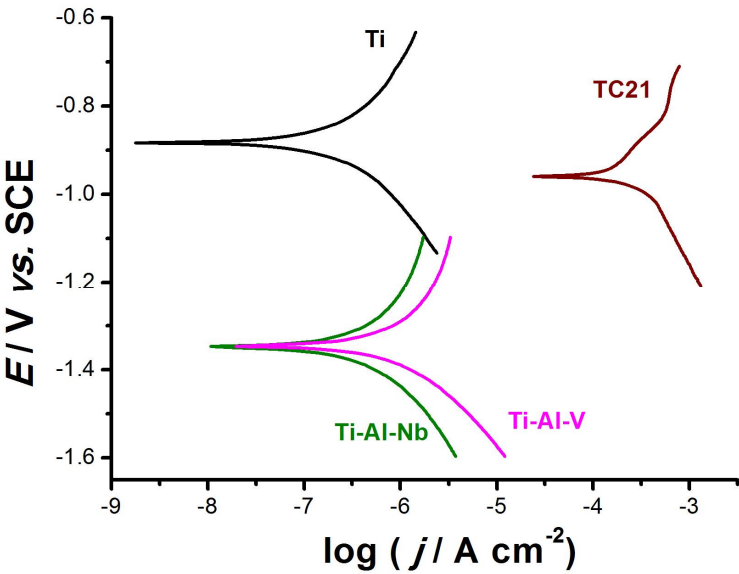309

310
311   **Figure 5 -** Cathodic and anodic polarization curves recorded for the three tested alloys in
312   comparison with pure Ti, after 7 days of exposure in 0.9% NaCl solution at a scan rate of 0.5 mV s^{-1} at
313   37 °C.
314
315   **Table 7 -** Mean values of the various electrochemical parameters obtained from Tafel extrapolation
316   method for pure Ti and the three tested alloys after 7 days of exposure in 0.9% NaCl solution at 37 °C.

Tested alloy	E_{corr} / mV(SCE)	β_c / mV dec^{-1}	β_a / mV dec^{-1}	j_{corr} / mA cm^{-2}
Pure Ti	-880	-296	400	3.4×10^{-4}
Ti-Al-Nb	-1350	-120	240	5×10^{-4}
Ti-Al-V	-1340	-240	480	10^{-3}
TC21	-960	-400	560	0.32

317
318   EIS measurements were also conducted at the respective E_{corr} throughout the exposure in 0.9%
319   NaCl solution at 37 °C to confirm the polarization data and to assess the kinetics of the uniform
320   corrosion process on the surfaces of the tested alloys. **Fig. 6** displays the impedance plots in Nyquist
321   projection, recorded for the studied alloys. Pure Ti (99.99%) was also included for comparison.
322   Plotting time of exposure on X-axis of impedance diagrams allowed for monitoring of uniform
323   corrosion susceptibility [31–33]. It can be observed that in each case the impedance spectra recorded
324   at day 1 (after initial 120 min of conditioning) were highly scattered due to non-stationary conditions
325   at the metal/electrolyte interface, which is a common problem in EIS measurements. This issue
326   became negligible after a few hours of exposure. For this reason, results recorded at day 2-7 will be

327 taken for further analysis. The impedance loop appeared as an open arc with a big diameter
328 (charge-transfer resistance, R_{ct}), hence the overall corrosion resistance of each investigated alloy is
329 very high. Ti-6Al-4V and Ti-6Al-7Nb alloys seem to be stable over time of the exposure, with
330 Ti-6Al-7Nb alloy being more corrosion resistant than Ti-6Al-4V alloy, while the results obtained for
331 TC21 reveal gradual decrease of the impedance loop, corroborating DC electrochemical studies.
332

333
334 **Figure 6 -** Nyquist impedance plots recorded for the three tested alloys in comparison with pure Ti
335 at the respective E_{corr} in 0.9 % NaCl solution at 37 °C. The changes in spectra shape with exposure
336 time (7 days) can be tracked on X-axis.
337

338   All impedance plots showed a single time constant (capacitive loop), which can be verified on
339 the corresponding Bode plots after 7 days of exposure (**Fig. 7**). An electric equivalent circuit (EEC)
340 was proposed to analyze the impedance results. Due to absence of additional time constants, a
341 simple Randles circuit was proposed with constant phase element (CPE) selected instead of
342 capacitance to take into consideration surface distribution of capacitance dispersion. The parallel
343 resistance represents the charge-transfer resistance R_{CT} through the metal/electrolyte interface *[34]*.
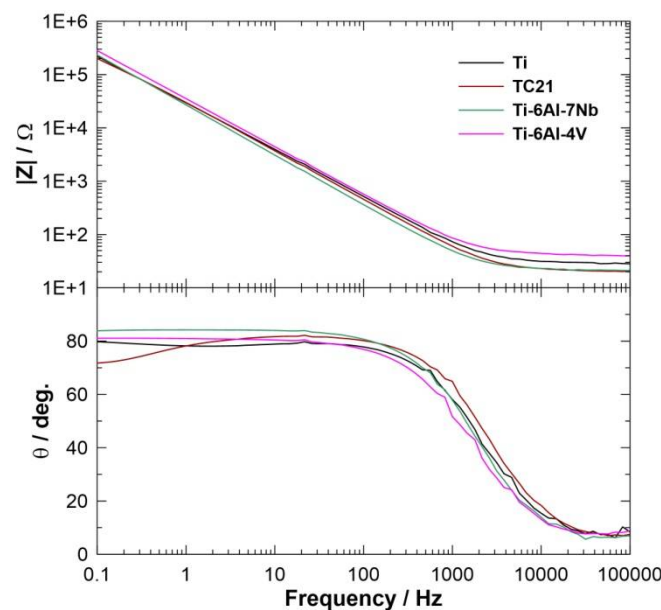344

345
346 **Figure 7 -** Bode plots of each investigated alloy on the day 7 of exposure in comparison with pure Ti
347 (99.99%) at the respective E_{corr} in 0.9 % NaCl solution at 37 °C.
348

349   The aforementioned capacitance dispersion may in particular originate from geometric
350 heterogeneity (pits, scratches, porosity) as well as diversified surface electric properties due to

351 adsorption processes of passive layer breakdown *[35]*. The CPE impedance $Z_{CPE} = (Q(j\omega)^n)^{-1}$
352 represents a capacitor with capacitance $1/Q$ for a homogeneous surface $n \to 1$. Thus, it is often
353 believed that CPE component n is the heterogeneity factor and its variation can be monitored. CPE
354 describes quasi-capacitive behaviour of passive layer in case of its double layer perforation. The
355 effective capacitance C_{eff} can be calculated on the base of CPE using Hirschorn's model for surface
356 distribution of time constants *[36]*. The EEC can be schematically written as $R_S(QR_{CT})$, where R_S is
357 electrolyte resistance. The aforementioned single time-constant EEC covers all the applied frequency
358 range.

359   **Fig. 8** depicts the electric parameters obtained on the base of $R_S(QR_{CT})$ EEC and their changes
360 during the one-week long exposure. The higher the R_{CT} the lower the corrosion current density,
361 offering an easy comparison in uniform corrosion resistance of investigated alloys, see **Fig. 8a**. Each
362 investigated alloy is characterized with very high resistance, range of MΩ, owing to a presence of a
363 passive layer tightly covering metal surface. Nevertheless, for TC21 alloy, R_{CT} value is one order of
364 magnitude lower and slowly but consistently decreases throughout the exposure, revealing its lower
365 corrosion resistance. High scatter of R_{CT} value is inversely proportional to measured fraction of
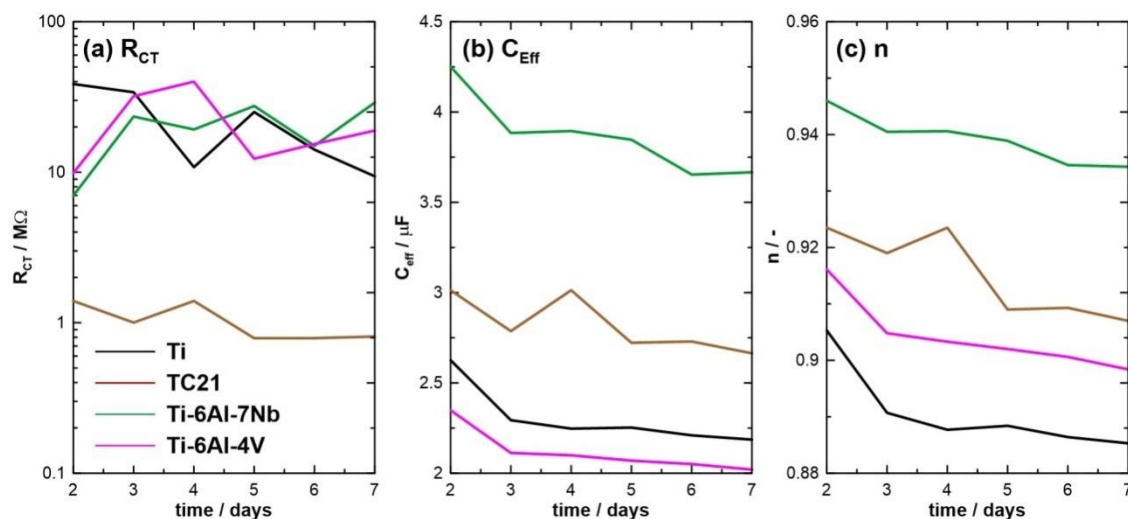366 impedance semicircle (as seen on **Fig. 6**).

367

369 **Figure 8 -** Charge transfer resistance R_{CT}, effective capacitance C_{eff} and CPE exponent n calculated on
370 the base of $R_S(QR_{CT})$ EEC for each investigated alloy. The one-week long exposure was carried out in
371 0.9 % NaCl solution at 37 °C.

372

373   The analysis of constant phase element (CPE) allows to draw conclusions on passive layer
374 homogeneity. The effective capacitance C_{eff}, calculated with surface distribution model is similar for
375 each investigated alloy, falling in a range between 2 and 5 µF. The differentiation may result from
376 differences in passive layer thickness d and to some extent from relative permittivity of alloying
377 additives and their oxides ε_r according to: $C = \varepsilon_0 \varepsilon_r d/A$, where ε_0 is the absolute permittivity and A is
378 the electrochemically active surface area. A steady decrease of C_{eff} should be attributed to an increase
379 of passive layer thickness, denouncing further passivation of metal in investigated electrolytic
380 conditions. The presence of stable corrosion pits would be visible in a form of rapid increase in C_{eff}
381 *[36,37]* (likely observed at TC21 alloy at day 4).

382   The initial value of CPE exponent n depends on factors such as surface phase distribution and
383 geometric defects remaining as a result of polishing. Its decrease throughout the exposure in
384 corrosive electrolyte reflects the appearance of heterogeneities on analyzed sample surface, which in
385 this case is primarily associated with initial phases of corrosion pits formation (see **Fig. 8c**). This
386 effect is clearly seen on SEM micrographs further in the manuscript. Notably, the value of n factor of
387 Ti-6Al-7Nb alloy was both: the highest as well as the least affected by exposure in corrosive media.
388 The aforementioned observation indicates high surface homogeneity, which may be the reason
389 behind outstanding corrosion resistance of this alloy.

390   3.3.2.Cyclic polarization measurements

391   **Figure 9** shows typical cyclic polarization curves in the linear (E vs. j) and logarithmic (E vs.
392   log j) formats recorded for the studied alloys between −2.0 V and +8.0 V (SCE). Measurements were
393   conducted in 0.9% NaCl solution at a scan rate of 5.0 mV s^{-1} at 37 ^{o}C. The logarithmic form of these
394   curves (E vs. log j), **Fig. 9 (b)**, is also constructed to define precisely the location of the pitting
395   potential (E_{pit}) and repassivation potential (E_{rp}) versus the corrosion potential (E_{corr}). **Fig. 9 (a₁)** is
396   zoomed with a very narrow range of current around the cathodic and anodic processes covering the
397   whole studied potential range to yield **Fig. 9 (a₂)**. It follows from **Fig. 9 (a₂)** that, for all tested
398   samples, the cathodic current density diminishes progressively reaching its zero value at the
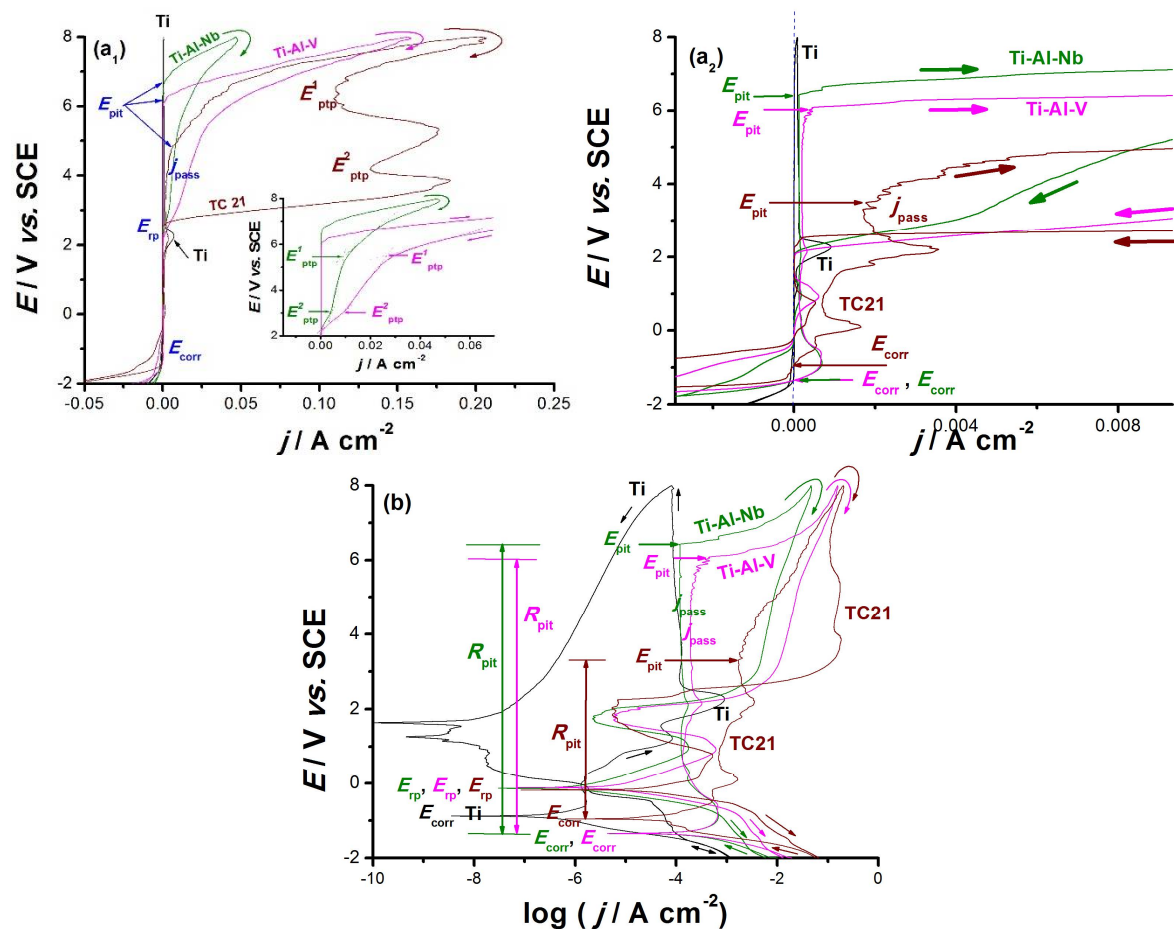399   corrosion potential (E_{corr}).

400

401

402
403   **Figure 9 -** Linear, **(a₁)** and **(a₂)**, and logarithmic **(b)** cyclic polarization curves recorded for the studied
404   alloys in 0.9% NaCl solutions at a scan rate of 1.0 mV s^{-1} at 37 ^{o}C.

405

406   The polarization curve of TC21 alloy exhibits active dissolution near E_{corr}, followed by an
407   obvious enhancement in the anodic current with the applied potential due to thinning and
408   weakening of the passive layer as a result of the aggressive attack of Cl$^-$ anions. Also, Ti-Al-Nb and
409   Ti-Al-V alloys show active dissolution near E_{corr}, but to a much lower extent than TC21, and in
410   addition, tend to passivate with a very low current (passive current, j_{pass}) covering a wide range of
411   potential. These findings reflect the weaker passivity of TC21 and its higher tendency to corrode in
412   this solution than Ti-Al-V and Ti-Al-Nb alloys. On the contrary, as expected, the anodic polarization
413   curve of pure Ti exhibits typical passivity near E_{corr}, referring to its high corrosion resistance.
414   Passivity of the studied alloys persists up to a certain critical potential, designated here as the
415   pitting potential (E_{pit}). Remarkable changes occurr within the passive region at potentials exceeding
416   E_{pit}. These involve a sudden increase in j_{pass} and formation of a hysteresis loop on the reverse

417 potential scan. These events are a clear sign for passivity breakdown, and initiation and propagation
418 of pitting corrosion.

419   In general, the electrochemical systems suffering from pitting corrosion are characterized by a
420 hysteresis loop in their cyclic voltammograms. Such a loop refers to the continuation of pitting
421 corrosion even after potential scan reversal (pitting corrosion's autocatalytic nature), indicating
422 repassivation delay of the existing pits. Repassivation is only achieved when the reverse scan
423 intersects the forward one within the passive region in a point designated here as the repassivation
424 potential, E_{rp}, below which the working electrode is immune against pitting. Others defined it as the
425 potential below which no pit could grow, or in other words, a pit once initiated, will stop *[38]*.

426   A current intermission can be seen on the reverse scan of the three tested alloys. This current
427 discontinuity is quite clear on the reverse scan of the TC21 alloy, and can be observed for alloys
428 Ti-Al-Nb and Ti-Al-V in the inset of **Fig. 9 (a₁)**. It takes place at two distinct potentials (E^1_{ptp} and E^2_{ptp}),
429 designated here as the pit transition potential (E_{ptp}), the potential between bare and salt-covered
430 state, where diffusion control dominates beyond E_{ptp} *[38]*. We previously reported similar findings
431 during pitting corrosion studies of Zn in nitrite solutions *[39]* and recently by Zakeri et al. *[40]*, who
432 explored the transition potential and the repassivation potential of AISI type 316 stainless steel in
433 chloride containing media devoid of and containing 0.01 M thiosulfate.

434   At potentials beyond E_{ptp}, the rate of anodic dissolution is diffusion-controlled (controlled by
435 diffusion of metal cations from the salt/pit solution interface into the bulk solution) *[38–40]*. Such a
436 current transient relationship, when satisfied, refers to an anodic diffusion control process *[40]*. On
437 reversing the potential scan, the thickness of the salt (pitting corrosion product) film diminishes.
438 This decrease in salt film thickness enhances with back scanning till a certain potential is reached at
439 which the cations' concentration decreases below the saturated concentration. At this stage, salt
440 precipitation is stopped, and the remaining metal salt film will be dissolved, making the bottom of
441 pits free from salt film. This in turn will establish an ohmic/activation control (a linear decrease of
442 current density with potential) regime.

443   Ti-Al-Nb alloy's passivity seems stronger and more stable that of the Ti-Al-V alloy, **Fig. 9 (b)**.
444 The latter is characterized by a higher j_{pass} which enhances with potential till its E_{pit}, which attained ~
445 50 mV vs. SCE before that of the former. In addition, the pits existing on the surface of Ti-Al-V alloy
446 find it much more difficult to repassivate than those on the surface of Ti-Al-Nb alloy, as the
447 hysteresis loop of the former is much larger than that of the later.

448   Another important pitting corrosion controlling electrochemical parameter is the pitting
449 corrosion resistance, R_{pit} (R_{pit} = |E_{corr} - E_{pit}|), which defines the resistance against the nucleation of
450 new pits [38]. Referring to **Fig. 9 (b)**, it is clear that R_{pit} increases following the order: TC21 ≪
451 Ti-Al-V < Ti-Al-Nb. The resistance against growth of the pits also controls the susceptibility toward
452 pitting corrosion. This can be evaluated via comparing the areas of the hysteresis loops formed
453 during the reverse potential scan of the cyclic polarization curves in its linear format, **Fig. 9 (a₁)**. A
454 specific routine of the Software was used to calculate the areas of the hysteresis loops, related to the
455 charge consumed during the growth of such already formed pits. Here again, the hysteresis loop of
456 the TC21 alloy recorded the highest area (charge consumed) among the studied alloys, while the
457 lowest value of the hysteresis loop's charge consumed during was measured for Ti-Al-Nb alloy.
458 This in turn ranks the resistance against the growth of pre-existing pits as Ti-Al-Nb > Ti-Al-V ≫
459 TC21. These findings mean that replacing V by Nb in Ti-Al-V alloy promotes alloy's repassivation
460 thus, enhancing its pitting corrosion resistance.

461 3.3.4.Chronoamperometry measurements

462   Chronoamperometry (*j/t*) measurements were also carried out to confirm the above results and
463 gain more information about the influence of alloyed V and Nb on the passive layer growth kinetics
464 and breakdown. **Figs. 10 (a) and 10 (b)** depict the *j/t* curves measured for the tested alloys at two
465 different E_a values, far below and close to E_b. Measurements were conducted in 0.9% NaCl solution
466 at 37 ºC. The profile of the obtained curves is found to vary according to the chemical composition of
467 the studied alloy and the position of E_a versus E_b. When E_a is located far cathodic to E_b, a *j/t* profile

468   with two stages is obtained, as shown in **Fig. 10 (a)**. During the first stage, the anodic current (j_a)
469   declines with a rate depending upon chemical composition of the tested alloy, denoting passive
470   layer electroformation and growth [39]. This decay in current then reaches a steady-state value (j_{ss}),
471   an almost constant passive current related to j_{pass} (revisit **Fig. 9**), constituting the 2nd stage of the
472   current. The constancy of j_{ss} originates from a balance between the rates of the passive layer growth
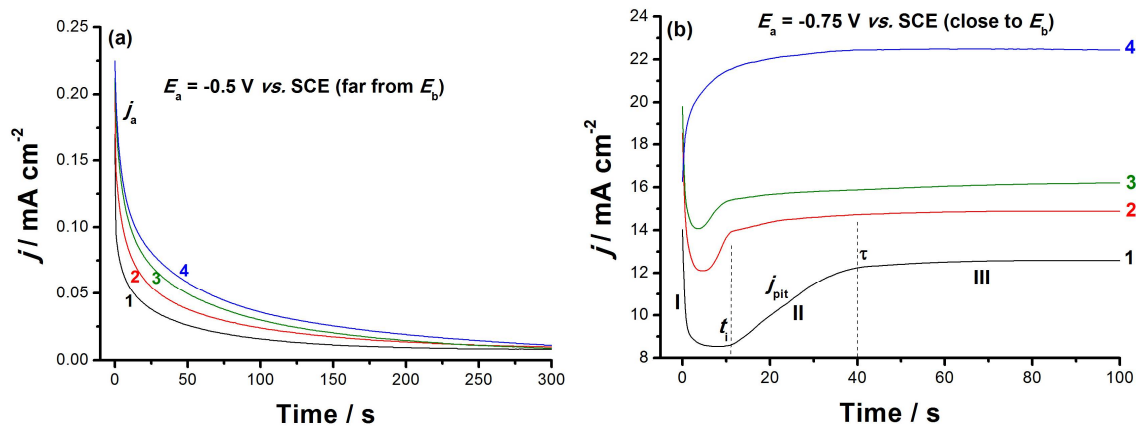473   (current builds up) and its dissolution (current decays) [41,42].
474

475
476   **Figure 10 -** Chronoamperometry (current - time) curves recorded for the studied solder alloys in
477   0.9% NaCl solution at applied anodic potentials of 2.0 and 4.0 V *vs.* SCE at 37 °C: (1) pure Ti; (2)
478   Ti-6Al-7Nb; (3) Ti-6Al-4V; (4) TC21.
479

480   Further snooping of **Fig. 10 (a)** demonstrates that the rate of j_a decay, and consequently the rate
481   of passive layer growth, diminishes upon alloying Ti with V and Nb. These results further confirm
482   the acceleration influence of the alloying elements V and Nb, with V being more active than Nb,
483   which when added to Ti weakened its passivity *via* depassivation (destabilizing the passive oxide
484   film through oxide film thinning/dissolution [43]). This in turn makes the passive film more
485   susceptible to pitting.
486   At the E_a value that is very close to E_b, **Fig. 10 (b)**, j/t curves with three different stages (I-III)
487   were obtained. Similar results were previously obtained in our lab [42,44]. Stage I referred to the
488   passive layer electroformation and growth, as its current falls with time [41,42,44]. This stage,
489   namely stage I ends at a certain time (t_i), the incubation time, where stage I's current reached its
490   minimum value; t_i is defined as the time the adsorbed aggressive Cl$^-$ anions must acquire to locally
491   attack and subsequently remove the passive oxide film [41]. The magnitude of t_i, more specifically its
492   reciprocal value ($1/t_i$), denotes the rate of pit initiation and growth [41,42], and measures the
493   susceptibility of the oxide film to breakdown and initiate pit formation and growth.
494   Stage II begins at t_i and terminates at another time τ, and its current is termed j_{pit} (pit growth
495   current density). j_{pit} increases from the moment just after t_i and continues in growth till τ, suggesting
496   that the pit formation and growth dominate over passivation during this stage. Ultimately, j_{pit}
497   attained a steady-state just after the time τ, denoting the onset of stage III, and continues almost
498   constant till the end of the run. The constancy of the stage III's current was attributed to the
499   hindrance of the current flow (j_{pit}) through the pits sealed off by the pitting corrosion products
500   formed during the events of stage II, namely pit initiation and growth [42,44]. This hindrance in j_{pit} is
501   balanced by a current increase due to metal dissolution, thus yielding an overall steady-state
502   current.
503   Close inspection of **Fig. 10** reveals that j_{pit} increases and t_i gets shorter, thus referring to
504   accelerated pitting attack, in presence of alloyed V. These results again support the catalytic impact
505   of alloyed V towards pitting corrosion

506   *3.4. Surface morphology and composition*

507   After one-week exposure, investigated samples were reexamined using SEM in order to
508 evaluate the susceptibility to pitting corrosion. This procedure was carried out after rinsing in
509 ethanol using ultrasonic cleaner. The results of the analysis are exhibited on **Fig. 11**. Defects start to
510 appear at the surface of each analyzed sample throughout the exposure. The micrographs in the
511 inset of **Fig. 11** were taken using back-scatter electrons (BSE) in topography mode. This allowed to
512 bring out the geometry of aforementioned defects. As can be seen, each analyzed defect forms shape
513 of a bulge above alloy's surface, testifying for either repassivation once formed shallow corrosion
514 pits or at an early, preliminary stage of passive layer degradation. Ti-6Al-4V sample is characterized
515 with both the highest amount and the largest defects, reaching 30 μm in diameter. On the other
516 hand, the surface of pure Ti and Ti-6Al-7Nb appeared the most intact. No real corrosion pits were
517 observed on the surface of either investigated alloy at the end of exposure in 0.9% NaCl solution at
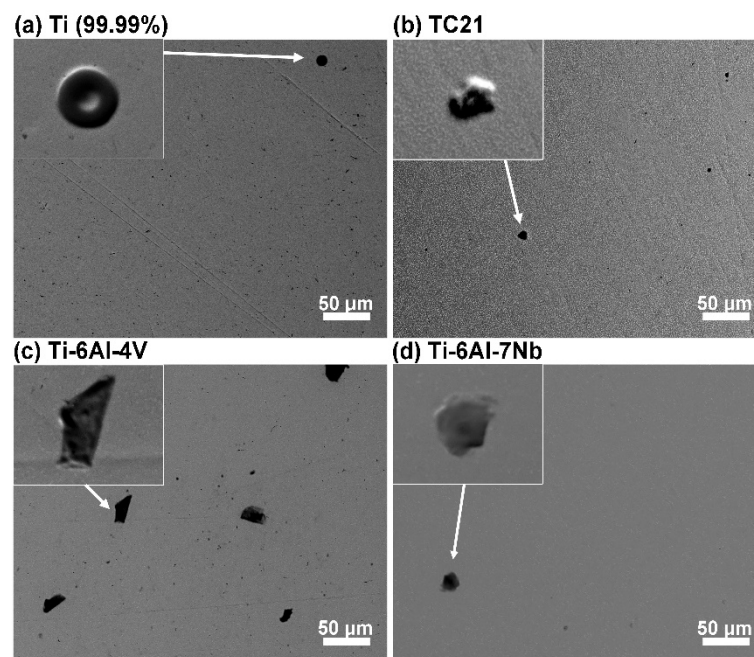518 37 °C, testifying for the overall high pitting corrosion resistance.
519

(a) Ti (99.99%)   **(b) TC21**   **(c) Ti-6Al-4V**   **(d) Ti-6Al-7Nb**

520
521 **Figure 11 -** SEM micrographs taken in secondary electron mode for each investigated sample: (a) pure Ti as a
522 reference, (b) TC21 alloy, (c) Ti-6Al-4V, (d) Ti-6Al-7Nb at the end of one-week long exposure in 0.9% NaCl at
523 37 °C. Magnification ×500. In the inset back-scatter electron topography mode images of selected surface
524 defects. Magnification ×2000.
525
526   Nevertheless, the passive layer must have weakened hence it was possible for corrosion
527 products to adsorb on the metal surface. EDS analysis was carried out for defects observed on each
528 investigated alloy in order to qualify their chemical constitution. The exemplary results, obtained for
529 Ti-6Al-7Nb alloy are summarized on **Figure S4** (**Supporting Information**), while the chemistry of
530 defects observed for each investigated alloy were similar. The defects are primarily composed of
531 carbon and oxygen, most likely forming metal carbonates typical for early pitting corrosion stages
532 *[45]*. Small amount of chlorine was also recorded within defects. Its low amount is distorted by EDS
533 depth of analysis ranging few microns.
534   The chemistry of the passive layer in each examined case is composed primarily of titanium (IV)
535 oxides, as verified by a strong recorded Ti_{2P} peak doublet, with $Ti_{2p3/2}$ component located each time at
536 458.6 eV *[35,46,47]*, **Fig. 12**. Furthermore, there is no sign of titanium oxides at lower oxidation states
537 corroborating the aforementioned result. Besides the titanium, other alloying additives also take part
538 in passivation process. The strongest signal among the alloying additives was recorded for
539 aluminum oxide Al_2O_3 ($Al_{2p3/2}$ peak at 74.5 eV), ranging between 3.5 and 3.8 at.% for each sample
540 *[48,49]*. The contribution of VO_2 ($V_{2p3/2}$ at 516.4 eV) in Ti-Al-V and Nb_2O_5 ($Nb_{3d5/2}$ at 207.1 eV) in
541 Ti-Al-Nb alloy did not exceed 0.7 at.% *[47,50,51]*. The passive film formed on the surface of TC21

542 alloy is naturally more complex. Besides TiO_2, it is composed of Al_2O_3 (3.8 at.%), Nb_2O_5 (0.3 at.%),
543 ZrO_2 (0.4 at.%, $Zr_{3d5/2}$ at 182.4 eV), Cr_2O_3 (0.8 at.%, $Cr_{2p3/2}$ at 576.0 eV), SnO_2 (0.1 at.%, $Sn_{3d3/2}$ at 486.5
544 eV), MoO_3 and MoO_2 (0.2+0.2 at.%, $Mo_{3d5/2}$ at 232.9 and 229.2 eV, respectively) *[52–55]*.
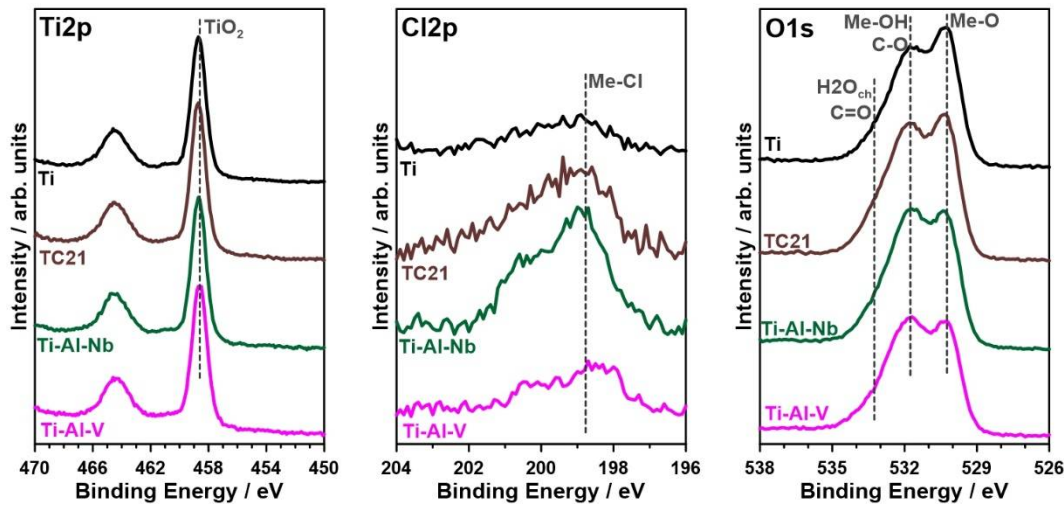545

546
547 **Figure 12 –** High-resolution XPS spectra recorded in Ti_{2p}, Cl_{2p} and O_{1s} energy range for each
548 investigated alloy after 7 days of exposure to 0.9% NaCl solution at 37 $^\circ$C.
549

550 The high-resolution spectra analysis carried out in the Cl_{2p} energy range confirms the
551 electrochemical and microscopic studies regarding chloride adsorption on the metal surface as a
552 result of 7-day metal exposure to chloride-containing electrolyte. Full chemical analysis is
553 summarized in **Table 8**. Metal chlorides were found on the surface of each investigated sample,
554 which confirms metal-chlorine covalent bond formation, testified by a peak doublet: $Cl_{2p3/2}$ at 198.9
555 eV *[35,42,56]*. Nevertheless, the amount of adsorbed chlorides is nearly 2.5 times higher for the TC21
556 alloy than pure titanium. The chloride concentration obtained for highly resistant Ti-Al-Nb alloy is
557 nearly on par with Ti sample, and slightly smaller than in the case of Ti-Al-V. An interesting
558 conclusion may be drawn based on O_{1s} peak analysis for each investigated sample. The spectra were
559 conventionally deconvoluted into three components. Two dominant components located at 530.2
560 and 531.6 eV are ascribed to Me-O and Me-OH species, respectively. The second component
561 intensity may be further influenced by presence of C-O bonds in carbonates. Its formation may result
562 from prolonged electrolyte exposure but also adventitious carbon formation due to air exposure
563 *[48,51]*. The finding regarding carbonates adsorption on the metal surface is further confirmed by
564 third O_{1s} component at 532.8 eV, typical for C=O bonds but also chemisorbed water molecules. For
565 clarity purposes the analysis excluded data recorded for carbon C_{1s}, which was found in large
566 amounts, up to 30 at.%, at binding energies corroborating adventitious carbon and carbonates
567 findings. Importantly, the highest amount of the adsorbed carbonate species was found on Ti-Al-V
568 sample surface, which is in very good agreement with SEM micrographs presented on **Fig. 11**. The
569 least amount of carbonate species was once more found on the surface of Ti sample.
570

571 **Table 8 –** XPS deconvolution results carried out in Ti_{2p}, Cl_{2p} and O_{1s} energy range after 7 days of
572 exposure to 0.9% NaCl solution at 37 $^\circ$C (in at.%).

	Ti_{2p}	other		O_{1s}		Cl_{2p}
	TiO_2	additives	Me-O	OH/CO	C=O/H_2O	Me-Cl
BE / eV	458.6	*	530.2	531.6	532.8	198.9
Ti	21.3	--	37.5	26.2	13.1	1.9
Ti-Al-V	17.4	4.3	28.8	25.7	20.8	3.0
Ti-Al-Nb	17.1	4.4	31.1	27.0	18.2	2.2
TC21	17.2	5.8	31.2	25.1	16.1	4.6

4. Conclusions

The effect of microstructure on the uniform and pitting corrosion characteristics of Ti-Al-V, and Ti-Al-Nb alloys is presented here. Pure Ti and TC21 alloy were included for comparison. Measurements were conducted in 0.9% NaCl solution at 37 ºC employing various electrochemical techniques, and complemented with XRD and SEM/EDS examinations. The obtained results revealed that:

1. The microstructure of the investigated alloys consists of α matrix, which was strengthened by β phase in all studied alloys except cp-Ti alloy.

2. The volume fraction of β phase in TC21 alloy is higher than in both Ti-Al-V and Ti-Al-Nb alloys. In comparison with other alloys, Ti-Al-Nb alloy has the lowest volume fraction of β phase.

3. Ti-Al-Nb alloy has the highest corrosion resistance among other alloys where it has the lowest corrosion rate.

4. The addition of Nb alloying element at the expense of V in Ti-Al-V alloy decreased the volume fraction of β phase, which improves the corrosion resistance of Ti based alloy.

5. The XPS results revealed adsorption of chloride and carbonate species on the surface of the investigated alloys, which amount is the lowest for cp-Ti and Ti-Al-Nb alloys, affecting the observed corrosion resistance.

6. Corrosion studies revealed that the uniform and pitting corrosion rates increase following the sequence: Ti < Ti-Al-Nb < Ti-Al-V < TC21.

References

1. Assis, S.L. de; Wolynec, S.; Costa, I. Corrosion characterization of titanium alloys by electrochemical techniques. *Electrochimica Acta* **2006**, *51*, 1815–1819.

2. Geetha, M.; Singh, A.K.; Asokamani, R.; Gogia, A.K. Ti based biomaterials, the ultimate choice for orthopaedic implants – A review. *Progress in Materials Science* **2009**, *54*, 397–425.

3. Jiang, H. Enhancement of Titanium Alloy Corrosion Resistance via Anodic Oxidation Treatment. *International Journal of Electrochemical Science* **2018**, 3888–3896.

4. Moiseyev, V.N. *Titanium alloys: Russian aircraft and aerospace applications*; Advances in metallic alloys; Taylor & Francis: Boca Raton, 2006; ISBN 978-0-8493-3273-9.

5. *Titanium and titanium alloys: fundamentals and applications*; Leyens, C., Peters, M., Eds.; Wiley-VCH ; John Wiley] (distributor): Weinheim : [Chichester, 2003; ISBN 978-3-527-30534-6.

6. Lütjering, G.; Williams, J.C. *Titanium: with 51 tables*; Springer-Verlag: Berlin, Heidelberg, 2007; ISBN 978-3-540-71397-5.

7. Oberwinkler, B.; Riedler, M.; Eichlseder, W. Importance of local microstructure for damage tolerant light weight design of Ti–6Al–4V forgings. *International Journal of Fatigue* **2010**, *32*, 808–814.

8. Knobbe, H.; Köster, P.; Christ, H.-J.; Fritzen, C.-P.; Riedler, M. Initiation and propagation of short fatigue cracks in forged Ti6Al4V. *Procedia Engineering* **2010**, *2*, 931–940.

618 9.   Fekry, A.M.; El-Sherif, R.M. Electrochemical corrosion behavior of magnesium and titanium alloys in
619   simulated body fluid. *Electrochimica Acta* **2009**, *54*, 7280–7285.

620 10.   Whittaker, M. Titanium Alloys. *Metals* **2015**, *5*, 1437–1439.

621 11.   Mountford Jr., J.A. Titanium - Properties, Advantages and Applications Solving the Corrosion Problems
622   in Marine Service. *NACE International* **2002**.

623 12.   Al-Mayouf, A..; Al-Swayih, A..; Al-Mobarak, N..; Al-Jabab, A.. Corrosion behavior of a new titanium
624   alloy for dental implant applications in fluoride media. *Materials Chemistry and Physics* **2004**, *86*, 320–329.

625 13.   García, C.; Ceré, S.; Durán, A. Bioactive coatings deposited on titanium alloys. *Journal of Non-Crystalline*
626   *Solids* **2006**, *352*, 3488–3495.

627 14.   Sharma, A.K. Anodizing titanium for space applications. *Thin Solid Films* **1992**, *208*, 48–54.

628 15.   Barjaktarević, D.R.; Cvijović-Alagić, I.L.; Dimić, I.D.; Đokić, V.R.; Rakin, M.P. Anodization of Ti-based
629   materials for biomedical applications: A review. *Metallurgical and Materials Engineering* **2016**, *22*, 129–144.

630 16.   Hines, J.A.; Lutjering, G. Propagation of microcracks at stress amplitudes below the conventional fatigue
631   limit in Ti-6Al-4V. *Fatigue <html_ent glyph="@amp;" ascii="&"/> Fracture of Engineering Materials and*
632   *Structures* **1999**, *22*, 657–665.

633 17.   Sieniawski, J.; Ziaja, W.; Kubiak, K.; Motyk, M. Microstructure and Mechanical Properties of High
634   Strength Two-Phase Titanium Alloys. In *Titanium Alloys - Advances in Properties Control*; Sieniawski, J.,
635   Ed.; InTech, 2013 ISBN 978-953-51-1110-8.

636 18.   Gai, X.; Bai, Y.; Li, J.; Li, S.; Hou, W.; Hao, Y.; Zhang, X.; Yang, R.; Misra, R.D.K. Electrochemical
637   behaviour of passive film formed on the surface of Ti-6Al-4V alloys fabricated by electron beam melting.
638   *Corrosion Science* **2018**, *145*, 80–89.

639 19.   Dadé, M.; Esin, V.A.; Nazé, L.; Sallot, P. Short- and long-term oxidation behaviour of an advanced
640   Ti2AlNb alloy. *Corrosion Science* **2019**, *148*, 379–387.

641 20.   Reda, R.; Nofal, A.; Hussein, A.-H. Effect of Single and Duplex Stage Heat Treatment on the
642   Microstructure and Mechanical Properties of Cast Ti–6Al–4V Alloy. *Metallography, Microstructure, and*
643   *Analysis* **2013**, *2*, 388–393.

644 21.   Nader El-Bagoury*, K.M.I. Microstructure, Phase Transformations And Mechanical Properties Of
645   Solution Treated Bi-Modal Titanium Alloy. *International Journal of Engineering Science and Research*
646   *Technology* **2016**.

647 22.   Zhao, X.; Sun, S.; Wang, L.; Liu, Y.; He, J.; Tu, G. A New Low-Cost β-Type High-Strength Titanium
648   Alloy with Lower Alloying Percentage for Spring Applications. *MATERIALS TRANSACTIONS* **2014**, *55*,
649   1455–1459.

650 23.   Phukaoluan, A.; Khantachawana, A.; Dechkunakorn, S.; Anuwongnukroh, N.; Santiwong, P.;
651   Kajornchaiyakul, J. Effect of Cu and Co Additions on Corrosion Behavior of NiTi Alloys for Orthodontic
652   Applications. *Advanced Materials Research* **2011**, *378–379*, 650–654.

653 24.   Lee, C.S.; Won, J.W.; Lee, Y.; Yeom, J.-T.; Lee, G.Y. High Temperature Deformation Behavior and
654   Microstructure Evolution of Ti-4Al-4Fe-0.25Si Alloy. *Korean Journal of Metals and Materials* **2016**, *54*,
655   338–346.

656 25.   ICDD: PDF 2, Database Sets 1-45; The International Centre for Diffraction Data, PA, USA 1995.

657 26.   Lutterotti, L.; Scardi, P. Simultaneous structure and size–strain refinement by the Rietveld method.
658   *Journal of Applied Crystallography* **1990**, *23*, 246–252.

659   27.   Lutterotti, L. Total pattern fitting for the combined size–strain–stress–texture determination in thin film
660   diffraction. *Nuclear Instruments and Methods in Physics Research Section B: Beam Interactions with Materials*
661   *and Atoms* **2010**, *268*, 334–340.

662   28.   ICSD database, Version 2005-1; Fachinformationszentrum Karlsruhe, Germany, and the U.S. Department
663   of Commerce, USA 2005.

664   29.   Dollase, W.A. Correction of intensities for preferred orientation in powder diffractometry: application of
665   the March model. *Journal of Applied Crystallography* **1986**, *19*, 267–272.

666   30.   Will, G.; Bellotto, M.; Parrish, W.; Hart, M. Crystal structures of quartz and magnesium germanate by
667   profile analysis of synchrotron-radiation high-resolution powder data. *Journal of Applied Crystallography*
668   **1988**, *21*, 182–191.

669   31.   Krakowiak, S.; Darowicki, K.; Ślepski, P. Impedance of metastable pitting corrosion. *Journal of*
670   *Electroanalytical Chemistry* **2005**, *575*, 33–38.

671   32.   Darowicki, K.; Krakowiak, S.; Slepski, P. The time dependence of pit creation impedance spectra.
672   *Electrochemistry Communications* **2004**, *6*, 860–866.

673   33.   Gerengi, H.; Slepski, P.; Ozgan, E.; Kurtay, M. Investigation of corrosion behavior of 6060 and 6082
674   aluminum alloys under simulated acid rain conditions: Corrosion behavior of 6060 and 6082 Al alloys
675   under acid rain. *Materials and Corrosion* **2015**, *66*, 233–240.

676   34.   Jorcin, J.-B.; Orazem, M.E.; Pébère, N.; Tribollet, B. CPE analysis by local electrochemical impedance
677   spectroscopy. *Electrochimica Acta* **2006**, *51*, 1473–1479.

678   35.   Alqarni, N.D.; Wysocka, J.; El-Bagoury, N.; Ryl, J.; Amin, M.A.; Boukherroub, R. Effect of cobalt addition
679   on the corrosion behavior of near equiatomic NiTi shape memory alloy in normal saline solution:
680   electrochemical and XPS studies. *RSC Advances* **2018**, *8*, 19289–19300.

681   36.   Hirschorn, B.; Orazem, M.E.; Tribollet, B.; Vivier, V.; Frateur, I.; Musiani, M. Determination of effective
682   capacitance and film thickness from constant-phase-element parameters. *Electrochimica Acta* **2010**, *55*,
683   6218–6227.

684   37.   Krakowiak, S.; Darowicki, K.; Slepski, P. Impedance investigation of passive 304 stainless steel in the pit
685   pre-initiation state. *Electrochimica Acta* **2005**, *50*, 2699–2704.

686   38.   Dong, Z.H.; Shi, W.; Guo, X.P. Initiation and repassivation of pitting corrosion of carbon steel in
687   carbonated concrete pore solution. *Corrosion Science* **2011**, *53*, 1322–1330.

688   39.   Amin, M.A.; Hassan, H.H.; Abd El Rehim, S.S. On the role of NO_2^- ions in passivity breakdown of Zn in
689   deaerated neutral sodium nitrite solutions and the effect of some inorganic inhibitors. *Electrochimica Acta*
690   **2008**, *53*, 2600–2609.

691   40.   Zakeri, M.; Naghizadeh, M.; Nakhaie, D.; Moayed, M.H. Pit Transition Potential and Repassivation
692   Potential of Stainless Steel in Thiosulfate Solution. *Journal of The Electrochemical Society* **2016**, *163*,
693   C275–C281.

694   41.   Amin, M.A.; Abd El-Rehim, S.S.; Aarão Reis, F.D.A.; Cole, I.S. Metastable and stable pitting events at zinc
695   passive layer in alkaline solutions. *Ionics* **2014**, *20*, 127–136.

696   42.   Amin, M.A.; El-Bagoury, N.; Mahmoud, M.H.H.; Hessien, M.M.; Abd El-Rehim, S.S.; Wysocka, J.; Ryl, J.
697   Catalytic impact of alloyed Al on the corrosion behavior of $Co_{50}Ni_{23}Ga_{26}Al_{1.0}$ magnetic shape memory
698   alloy and catalysis applications for efficient electrochemical H_2 generation. *RSC Advances* **2017**, *7*,
699   3635–3649.

700   43.   Amin, M.A.; Fadlallah, S.A.; Alosaimi, G.S. Activation of Titanium for Synthesis of Supported and
701   Unsupported Metallic Nanoparticles. *Journal of The Electrochemical Society* **2014**, *161*, D672–D680.

44. Amin, M.A.; Abd El-Rehim, S.S.; El-Sherbini, E.E.F.; Mahmoud, S.R.; Abbas, M.N. Pitting corrosion studies on Al and Al–Zn alloys in SCN− solutions. *Electrochimica Acta* **2009**, *54*, 4288–4296.

45. Scully, J.R. Localized Corrosion of Sputtered Aluminum and Al-0.5% Cu Alloy Thin Films in Aqueous HF Solution. *Journal of The Electrochemical Society* **1990**, *137*, 1365.

46. Pouilleau, J.; Devilliers, D.; Garrido, F.; Durand-Vidal, S.; Mahé, E. Structure and composition of passive titanium oxide films. *Materials Science and Engineering: B* **1997**, *47*, 235–243.

47. Milošev, I.; Kosec, T.; Strehblow, H.-H. XPS and EIS study of the passive film formed on orthopaedic Ti–6Al–7Nb alloy in Hank's physiological solution. *Electrochimica Acta* **2008**, *53*, 3547–3558.

48. Wysocka, J.; Cieslik, M.; Krakowiak, S.; Ryl, J. Carboxylic acids as efficient corrosion inhibitors of aluminium alloys in alkaline media. *Electrochimica Acta* **2018**, *289*, 175–192.

49. Amin, M.A.; Ahmed, E.M.; Mostafa, N.Y.; Alotibi, M.M.; Darabdhara, G.; Das, M.R.; Wysocka, J.; Ryl, J.; Abd El-Rehim, S.S. Aluminum Titania Nanoparticle Composites as Nonprecious Catalysts for Efficient Electrochemical Generation of H$_2$. *ACS Applied Materials & Interfaces* **2016**, *8*, 23655–23667.

50. Weibin, Z.; Weidong, W.; Xueming, W.; Xinlu, C.; Dawei, Y.; Changle, S.; Liping, P.; Yuying, W.; Li, B. The investigation of NbO$_2$ and Nb$_2$O$_5$ electronic structure by XPS, UPS and first principles methods: The investigation of NbO2 and Nb2O5 electronic structure. *Surface and Interface Analysis* **2013**, *45*, 1206–1210.

51. Kharitonov, D.S.; Sommertune, J.; Örnek, C.; Ryl, J.; Kurilo, I.I.; Claesson, P.M.; Pan, J. Corrosion inhibition of aluminium alloy AA6063-T5 by vanadates: Local surface chemical events elucidated by confocal Raman micro-spectroscopy. *Corrosion Science* **2019**, *148*, 237–250.

52. Kumar, S.; Kumar, S.; Tiwari, S.; Srivastava, S.; Srivastava, M.; Yadav, B.K.; Kumar, S.; Tran, T.T.; Dewan, A.K.; Mulchandani, A.; et al. Biofunctionalized Nanostructured Zirconia for Biomedical Application: A Smart Approach for Oral Cancer Detection. *Advanced Science* **2015**, *2*, 1500048.

53. Siuzdak, K.; Szkoda, M.; Karczewski, J.; Ryl, J.; Darowicki, K.; Grochowska, K. Fabrication and Significant Photoelectrochemical Activity of Titania Nanotubes Modified with Thin Indium Tin Oxide Film. *Acta Metallurgica Sinica (English Letters)* **2017**, *30*, 1210–1220.

54. Mandrino, D.; Godec, M.; Torkar, M.; Jenko, M. Study of oxide protective layers on stainless steel by AES, EDS and XPS. *Surface and Interface Analysis* **2008**, *40*, 285–289.

55. Wang, C.; Irfan, I.; Liu, X.; Gao, Y. Role of molybdenum oxide for organic electronics: Surface analytical studies. *Journal of Vacuum Science & Technology B, Nanotechnology and Microelectronics: Materials, Processing, Measurement, and Phenomena* **2014**, *32*, 040801.

56. Liu, J.; Alfantazi, A.; Asselin, E. Effects of Temperature and Sulfate on the Pitting Corrosion of Titanium in High-Temperature Chloride Solutions. *Journal of The Electrochemical Society* **2015**, *162*, C189–C196.